

Full length article

Imparted benefits on mechanical properties by achieving grain boundary migration across voids

Wei Wang^a, Daniel S Balint^a, Amir A Shirzadi^b, Yaping Wang^a, Junyi Lee^a, Lee Aucott^c, Jun Jiang^{a,*}

^a Department of Mechanical Engineering, Imperial College London, London, SW7 2AZ, UK

^b School of Engineering and Innovation, The Open University, Milton Keynes MK7 6AA, UK

^c United Kingdom Atomic Energy Authority, Culham Centre for Fusion Energy, Culham Science Centre, Abingdon, Oxon OX14 3DB, UK

ARTICLE INFO

Keywords:

Grain boundary
Void
Crystal plasticity
Diffusion bonding

ABSTRACT

Understanding the interaction of micro-voids and grain boundaries is critical to achieving superior mechanical properties for safety-critical parts. Micro-voids and grain boundaries may interact during advanced manufacturing processes such as sintering, additive manufacturing and diffusion bonding. Here, we show imparted benefits on mechanical properties by achieving grain boundary migration across voids. The micro-mechanisms and quantitative analysis of grain boundary migration on local deformation were studied by integrated in-situ EBSD/FSE and crystal plasticity finite element modelling. It is revealed that a migrated grain boundary does not alter the activated slip systems but precludes grain boundary-multislip interaction around interfacial voids to alleviate stress concentrations. The stress mitigation caused by grain boundary migration is almost the same as that caused by void closure under the example diffusion bonding thermal-mechanical process used in this study. This new understanding sheds light on the mechanistic link between GND hardening, grain boundary migration and the corresponding material tensile behaviour. It opens a new avenue for achieving superior mechanical properties for metallic parts with micro-defects such as those generated in diffusion-bonded, sintered and additive manufactured components.

1. Introduction

Safety critical components fabricated by additive manufacturing (AM), powder metallurgy (PM) and solid-state bonding have been used in aerospace [1], atomic energy [2] and mobile communication [3]. However, even though advanced process designs are used in fabrication, micro-defects, e.g., voids, are still inevitable, limiting the components' reliability. The generation and evolution of micro-defects in such fabrication technologies are not independent but rather simultaneous processes coupled to grain boundaries (GBs) migration. The complex GBs and micro-void interactions under processing conditions make understanding the underlying mechanisms difficult. Yet, a fundamental understanding of evolving micro-voids and GBs on deformation behaviour is essential to engineer microstructures for enhanced reliability of those parts.

Micro-voids, GBs and their complex interaction are ubiquitous in AM, sintering [4], diffusion bonding (DB) [5,6] and other manufacturing processes. For example, micro-voids are the most

common defects in additive-manufactured metallic parts [7], often due to entrapped gas, keyholing or lack of fusion [8]. Voids also can be found at the GB in precipitation-hardened aluminium alloys [9]. Experimentally, it is impossible to control and investigate the individual role of any one feature (e.g., void and GB migration) on the fracture mechanism since these features are inherently coupled. Previous experimental results have correlated void closure and GB migration with DB parameters such as temperature [10,11], time [12,13], pressure [14,15] and surface condition [16,17]. The void sizes are reduced during the DB process while the interfacial GBs migrate across the voids, resulting in the voids sitting at GBs or being included within grains. GB manifests its ability to modulate the mechanical properties of crystalline materials through the GB strengthening mechanism [18]. In contrast, voids, causing stress concentration under loading, are one of the primary factors responsible for the deformation and fracture of materials [19]. The corresponding mechanisms have been extensively studied in [9,20–26]. However, their complex interactions are rarely mentioned.

In this work, we aim to systematically investigate the effects of GB

* Corresponding author.

E-mail address: jun.jiang@imperial.ac.uk (J. Jiang).

<https://doi.org/10.1016/j.actamat.2023.119103>

Received 8 March 2023; Received in revised form 7 June 2023; Accepted 19 June 2023

Available online 19 June 2023

1359-6454/Crown Copyright © 2023 Published by Elsevier Ltd on behalf of Acta Materialia Inc. This is an open access article under the CC BY license (<http://creativecommons.org/licenses/by/4.0/>).

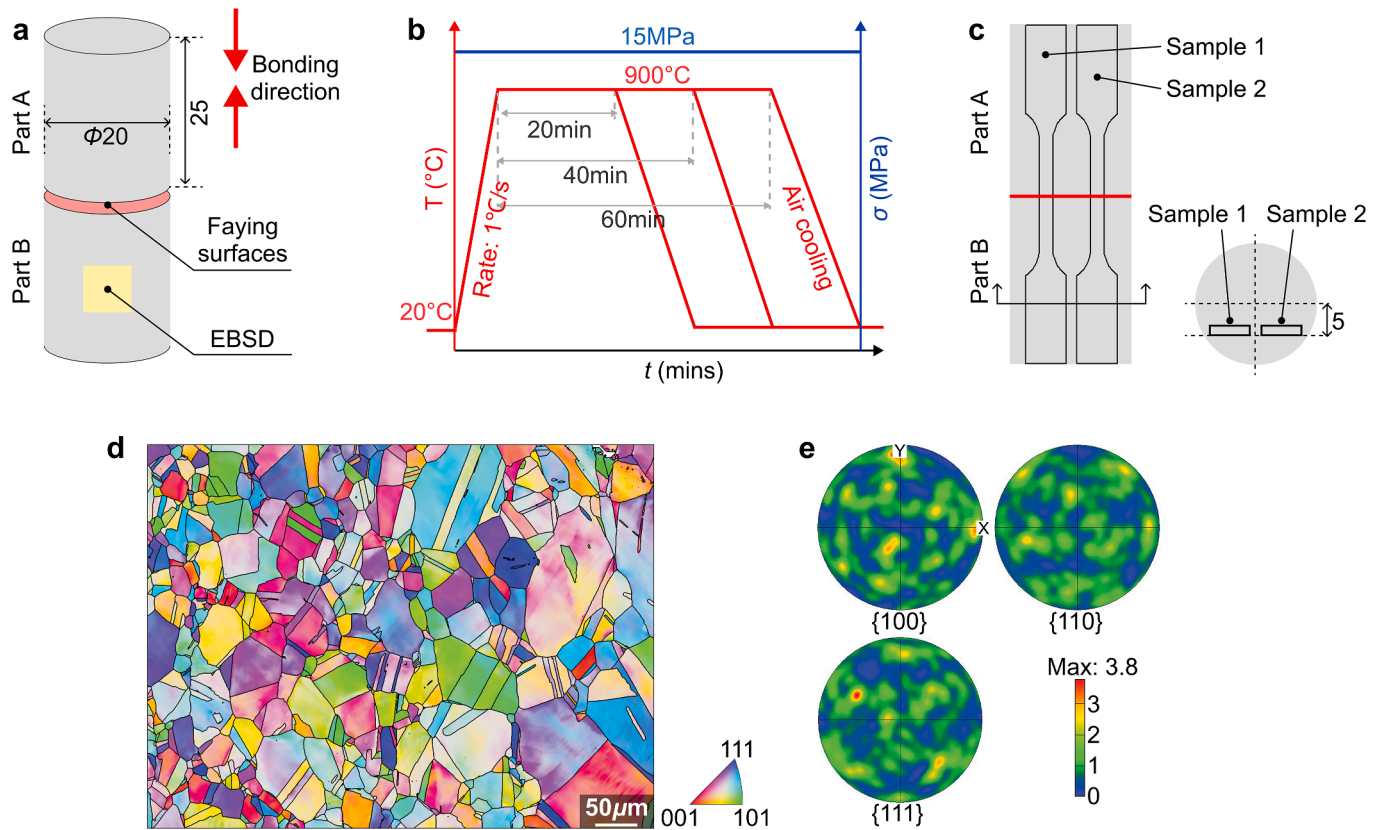


Fig. 1. Sample preparation and DB test: (a) dimensions of DB sample, (b) temperature history of DB, (c) tensile samples for tensile tests, (d) EBSD microstructure and (e) corresponding pole figure.

Table 1
DB conditions.

Case	Bonding Temperature (°C)	Bonding Time (mins)
A	900	20
B	900	40
C	900	60
D	800	60
E	1000	60

migration on deformation in the vicinity of voids. A newly established integrated micromechanical testing, characterisation and modelling methodology was used. In-situ foreshattered electron (FSE), electron backscatter diffraction (EBSD) characterisation and physical-based crystal plasticity finite element (CPFE) modelling were adopted. Two 316 L cylindrical samples with deliberately designed GBs and voids were diffusion bonded, during which microstructure evolution only occurs near the DB interface. The DBed samples were then in-situ tensile tested. The slip activation and deformation at the grain level were observed. The cases with and without GB migration across the voids, defined as intragranular and intergranular voids, were compared, and the results show evidence of GB migration on local stress mitigation. Meanwhile, dislocation-based microstructure-governed bi-crystal CPFE models were developed and validated. A novel voids-GB interaction mechanism was established to show how local stress was mitigated by GB migration.

2. Methodology

2.1. Sample preparation

As-received 316 L samples were diffusion-bonded using the cycle shown in Fig. 1. The bonding temperature and time used in this work are

given in Table 1. The faying surfaces of all samples were polished using 1200 Grit SiC emery papers and rinsed in propanolol before loading in the diffusion bonding equipment. The diffusion bonding was conducted in a vacuum with a pressure of about 5×10^{-4} mbar. The samples were held under a compressive pressure of 15 MPa throughout the bonding cycle. The use of a high vacuum condition and considerable contact pressure in this work guarantees that no oxide scale remains at the interface after bonding [27]. The influence of interfacial oxide scales on the local deformation is thus ignored. Microstructure details of as-received 316 L are shown in Fig. 1d, which indicates large grains with a size of about $22\mu\text{m}$. The corresponding pole figure (PF) shown in Fig. 1e indicates little texture for the steel.

2.2. In-situ SEM/EBSD investigation

Dog-bone-shaped tensile samples were cut from the DB samples by electrical discharge machining (EDM) with gauge dimensions of 15 mm length, 2 mm width, and 1.8 mm thick, as shown in Fig. 1c. Tensile samples were metallographically ground by a series of SiC papers and finished with a $1\mu\text{m}$ diamond suspension. After mechanical polishing, the samples were electropolished for 60 s in a solution of 10 vol% perchloric acids in glacial acetic acid at room temperature under 25 V. In-situ tensile tests were performed at ambient temperature. The tensile tests were performed under displacement control at 0.45 mm/min. The CN Tech micro-mechanical tensile stage was used in a TESCAN CLARA SEM system. Electron backscattered diffraction (EBSD) was performed using the Oxford Instruments EBSD system. The test was interrupted at an increment of 25 MPa, so SEM images and EBSD maps could be captured for microstructure-deformation analysis. Fore-scattered electron (FSE) imaging with 4096×4096 resolution was recorded to identify the surface slip trace.

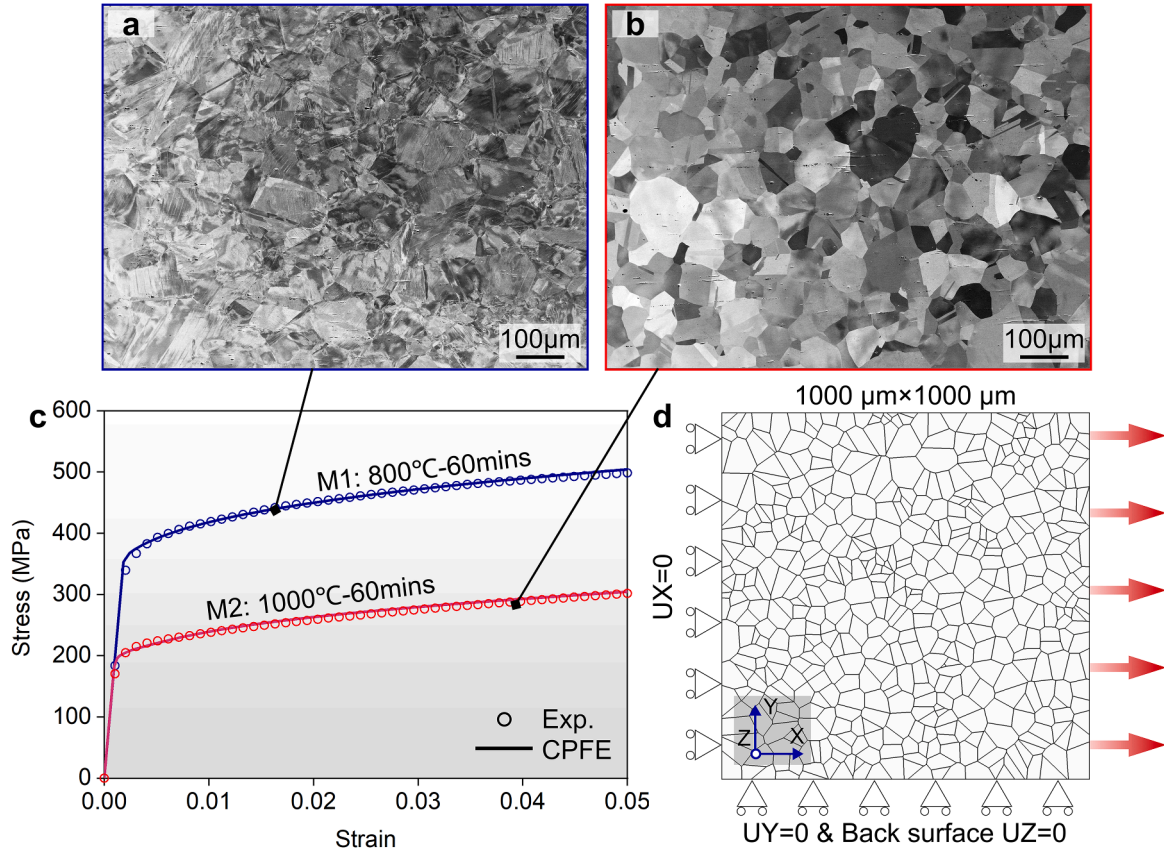


Fig. 2. Tensile behaviours of 316 L obtained by experiment and CPFE simulation (a) Microstructures after 800 °C-60mins and (b) 1000 °C-60mins anneal, (c) stress-strain curves correspond to the microstructures shown in Fig. 2a, b and (d) boundary conditions for CPFE uniaxial tensile simulation.

2.3. Dislocation-based crystal plasticity finite element (CPFE)

The deformation behaviours at the interface of DB 316 L are modelled by a dislocation-based CPFE [28,29]. The model can capture the individual slip activation to reveal the anisotropic plasticity. The geometrically necessary dislocations (GND) density can be obtained based on a physical calculation that reflects the curl of the plastic strain gradient. This further reveals the grain-size-dependent deformation behaviours [30]. The detailed descriptions are as follows.

The overall deformation gradient \mathbf{F} is multiplicatively decomposed into the elastic and plastic components

$$\mathbf{F} = \mathbf{F}^e \cdot \mathbf{F}^p \quad (1)$$

where \mathbf{F}^e is the elastic deformation gradient and \mathbf{F}^p is the plastic deformation gradient.

The plastic velocity gradient \mathbf{L}^p is the summation of the contribution of shear rates $\dot{\gamma}^\alpha$ from each slip system.

$$\mathbf{L}^p = \dot{\mathbf{F}}^p \mathbf{F}^{p-1} = \sum_{\alpha=1}^N \dot{\gamma}^\alpha \mathbf{s}^\alpha \otimes \mathbf{m}^\alpha \quad (2)$$

where \mathbf{s}^α represents slip direction and \mathbf{m}^α is the normal of slip plane for the slip system α . N represents the total number of slip systems. The selected 316 L steel has a face-centred cubic (FCC) crystal structure. Thus, the combination of $\{111\}\langle 110 \rangle$ of 12 different slip systems are considered.

The relationship between the slip rate $\dot{\gamma}^\alpha$ and the movement of dislocation is induced by a dislocation-based Orowan equation [31], such that the slip rate on an individual slip system α is determined by

$$\dot{\gamma}^\alpha = \rho_M b v^\alpha \quad (3)$$

where ρ_M is the mobile dislocation density, b is the magnitude of Burgers vector, v^α is the velocity of dislocations, which is determined by thermally activated dislocation escape from obstacles such as lattice defects. The slip rate $\dot{\gamma}^\alpha$ along the α slip system can be further expressed as

$$\dot{\gamma}^\alpha = \rho_M b^2 v_0 \exp\left(-\frac{\Delta F}{k_B T}\right) \sinh\left(\frac{\Delta V}{k_B T} \langle |\tau^\alpha| - \tau_c^\alpha \rangle\right) \quad (4)$$

where T is the loading temperature, k_B is the Boltzmann constant, v_0 is the jump frequency for dislocation escape, ΔF is the activation energy, ΔV is the activation volume, τ^α is the resolved shear stress and τ_c^α is the critical resolved shear stress. The shear strain rate $\dot{\gamma}^\alpha$ is only activated when resolved shear stress τ^α exceeds the critical resolved shear stress τ_c^α , that is, $|\tau^\alpha| - \tau_c^\alpha > 0$. Otherwise, $\dot{\gamma}^\alpha$ remains inactivated.

Taylor slip hardening rule is used for the evolution of critical resolved shear stress τ_c^α along α slip systems [32]

$$\tau_c^\alpha = \tau_{c0} + \mu G b \sqrt{\rho_{SSD} + \rho_{GND}} \quad (5)$$

where G is the shear modulus of the material, τ_{c0} is the initial critical resolved shear stress without dislocation density hardening, μ is the material constant. ρ_{GND} is the density of GND. ρ_{SSD} is the density of statistically stored dislocations (SSD) determined by an equation using effective plastic strain as [33]

$$\dot{\rho}_{SSD} = \lambda \dot{\rho} = \left(\frac{2}{3} \mathbf{D}^p : \mathbf{D}^p\right)^{1/2} \quad (6)$$

where λ is the hardening coefficient.

The density of GND is calculated based on Nye's tensor, in which local plastic strain gradients supporting the lattice curvature are used

Table 2

Physical properties for non-Rx grains and Rx grains in the CPFE model of 316 L steel.

	Material 1	Material 2
E (GPa)	207	207
G (GPa)	80	80
μ	0.39	0.31
ΔV (μm^3)	$39.37 \times b^3$	$39.37 \times b^3$
ΔF (J)	2.60×10^{-20}	2.60×10^{-20}
k_B (JK^{-1})	1.38×10^{-23}	1.38×10^{-23}
λ (μm^{-2})	175	175
τ_0^i (MPa)	158	82
b (μm)	2.50×10^{-4}	2.50×10^{-4}
ρ_M (μm^{-2})	1×10^{-2}	1×10^{-2}

$$\Lambda = \nabla \times \mathbf{F}^p = \sum_{i=1}^N \rho_{Gs}^\alpha \mathbf{b}^\alpha \otimes \mathbf{s}^\alpha + \rho_{Gct}^\alpha \mathbf{b}^\alpha \otimes \mathbf{t}^\alpha + \rho_{Gen}^\alpha \mathbf{b}^\alpha \otimes \mathbf{m}^\alpha \quad (7)$$

where ρ_{Gen}^i is the normal component of the edge dislocation density, ρ_{Gct}^i denotes the tangential component of the edge dislocation density, and ρ_{Gs}^i is the screw dislocation component.

There are 36 independent dislocation components corresponding to the 12 slip systems in FCC crystal. Eq. (7) then can be recast as

$$A\rho_G = \bar{\Lambda} \quad (8)$$

where $\bar{\Lambda}$ is the vectorised Nye's tensor, and A is a linear tensor. Because of the Eqn. (8) cannot be uniquely solved. The L2 norm method is used according to Ref. [34–36]

$$\rho_{GND} = \sqrt{\sum_{i=1}^N (\rho_{Gs}^\alpha)^2 + (\rho_{Gct}^\alpha)^2 + (\rho_{Gen}^\alpha)^2} \quad (9)$$

The dislocation-based crystal plasticity constitutive law was implemented as a UMAT subroutine of a finite element code ABAQUS.

2.4. Material properties calibration and model validation

The recrystallization (Rx) and non-Rx grains can be identified for all DB cases. The Rx grains would be generated during high-temperature DB-induced Rx, while non-Rx grains would be the residual grains from as-received materials. To calibrate CPFE parameters for these two kinds of grains, as-received 316 L was annealed at 800 °C and 1000 °C for 60mins to simulate the DB conditions and then strained under uniaxial tensile tests. The microstructures after annealing with full residual non-Rx grains (800 °C-60mins) and complete Rx grains (1000 °C-60mins) are shown in Fig. 2a and b, and the corresponding stress-strain curves are shown in Fig. 2c.

The uniaxial tensile simulations were then implemented by CPFE. The average grain size in CPFE was set to be the same as the characterisation results shown in Fig. 2a and b. A realistic grain-shape quasi-3D CPFE model was adopted [37], in which the grain morphology in the front surface was extruded along the third dimension to generate the 3D model. The boundary and loading conditions are shown in Fig. 2d. The displacement-control loading condition was applied to the right surface, which aims to replicate the loading scenarios in the tensile tests. The left, bottom and back surfaces were constrained by $U_x=0$, $U_y=0$ and $U_z=0$, respectively, while the front surface was free of constraint to achieve a plane stress condition [38]. Twenty-node 3D elements with reduced integration (C3D20R) [39] were used. The number of elements through thickness is fixed to be 4, as the model thickness and the number of elements through thickness have negligible effects on the stress and strain response on the front surface [40]. The physical properties for non-Rx grains and Rx grains (namely material 1 and material 2) obtained from Ref. [41] and simulations are listed in Table 2.

The CPFE-predicted stress-strain curves shown in Fig. 2c give reasonably good agreement with experimental data for both non-Rx grains and Rx grains. In addition, the EBSD-based CPFE simulations were conducted for DB specimens processed at 900 °C-40mins (Fig. 3). The results predicted by CPFE show good agreement with the in-situ FSE/EBSD for both cases.

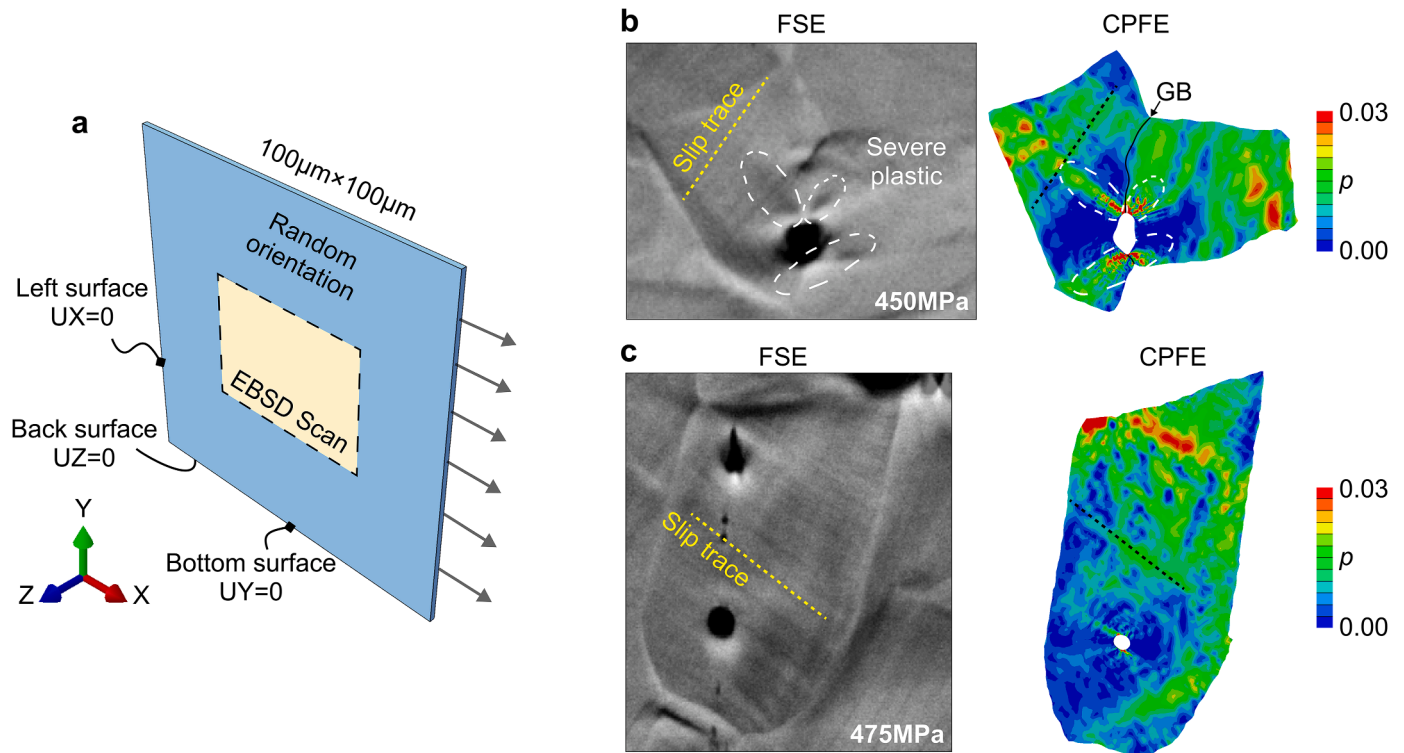


Fig. 3. CPFE model validation (a) boundary conditions, (b) and (c) comparison of local plasticity between FSE and EBSD in intergranular void and intragranular void. CPFE results obtained at engineering strain of 1%.

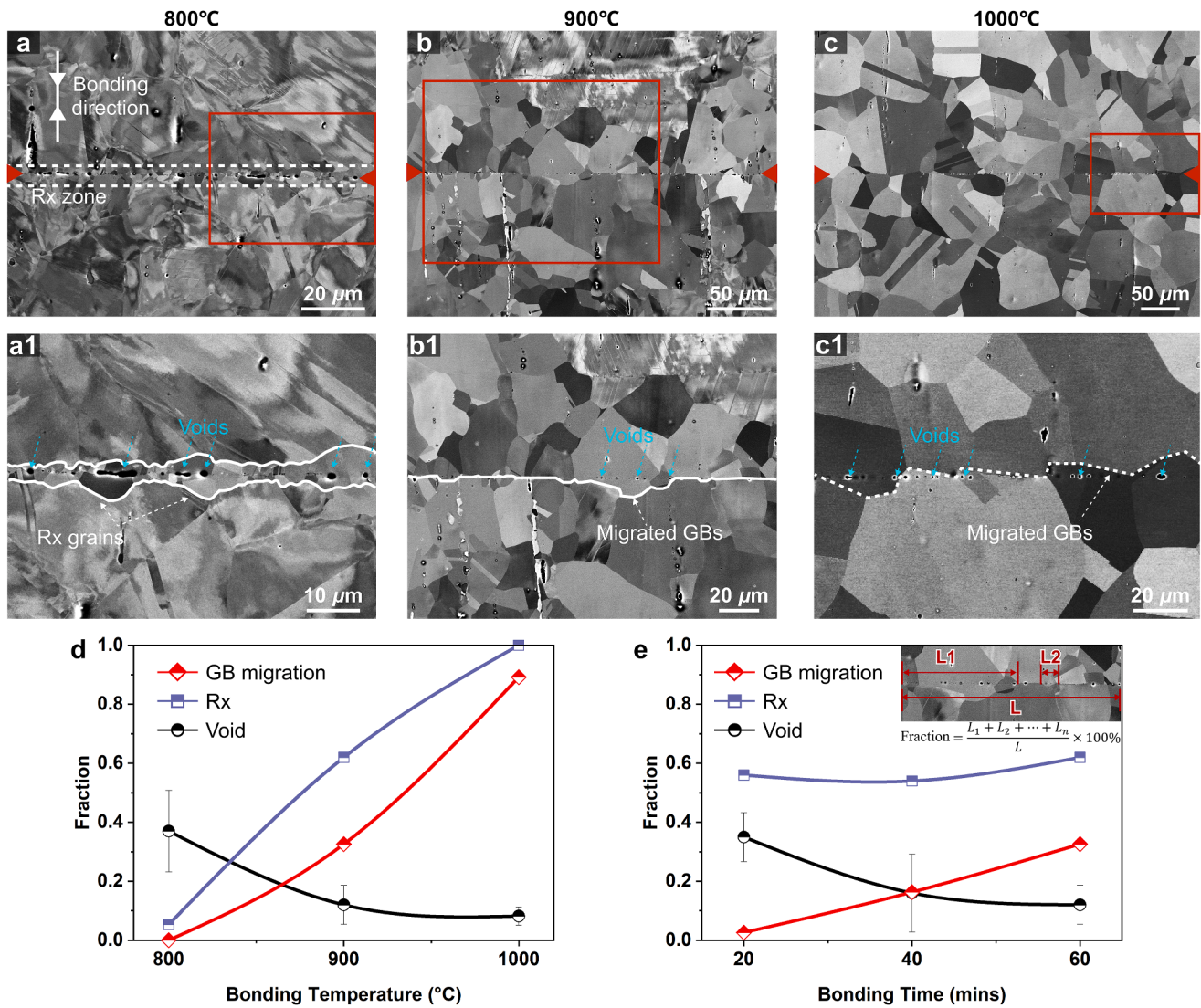


Fig. 4. Microstructure features at the bonding interface with bonding temperature increases (a) 800 °C-60mins; (b) 900 °C-60mins; and (c) 1000 °C-60mins; evolution of microstructure features with (d) temperature increases for 60mins DB and (e) time increases for 900 °C DB.

3. Results and discussions

3.1. As-fabricated microstructures

Fig. 4 shows the as-fabricated microstructure under three selected bonding temperatures. Under low-temperature DB, such as 800 °C (Fig. 4a), Rx appeared in a narrow region near the interface. This is most likely due to the deformation of asperities during contact or possibly the induced coldwork during the polishing of the faying surfaces. These two processes increase the interface's local dislocation density to promote the Rx at elevated temperatures during DB. The Rx is more pronounced at 900 °C, and coarser Rx grains appear near the interface and on the matrix (Fig. 4b). At 1000 °C, grains undergo complete Rx (Fig. 4c). The Rx and following grain growth promote the GB migration across voids. GB migration is first seen at 900 °C, as shown in Fig. 4b1. No GB migration was found at lower temperatures (800 °C) due to large size voids and insufficient GB mobility. It is clear that as the bonding temperature increases, a higher fraction of GB migration occurs (Fig. 4c1), resulting in more voids being included within grains' interior rather than at GBs.

The correlations of GB migration fraction, Rx area fraction and changing void ratio with bonding temperature and time are summarised

in Fig. 4d and e. It is noted that the speed of recrystallization is faster than that of the interfacial GB generation and migration. Thus, the GBs that deviate from the original bonding line are migrated GBs. The calculation method for GB migration fraction is shown in Fig. 4e. The rates of GB migration and void size seem predominately determined by the bonding temperature and time, though the Rx behaviour seems influenced mainly by the bonding temperature. The bonding temperature and time increases promote GB migration, Rx and void-size reduction.

3.2. Mechanical response and fracture behaviour

To clarify the effects of void and GB migration on deformation behaviours, the DB samples were fabricated at 900 °C for 20mins, 40mins and 60mins, and then uniaxial tensile tested to evaluate their interfacial strength. As shown in Fig. 5a, interfacial fracture (adhesive fracture) occurs in the 20 and 40mins bonded specimens, lacking the apparent necking stage in the tensile curve. However, the fracture position shifts from the interface to the matrix as the bonding dwell time increases to 60mins, indicating that 100% bonding strength is achieved.

Interestingly, for specimens under 900 °C-40mins DB, although the macro fracture occurs at the interface, some of the fracture surfaces at

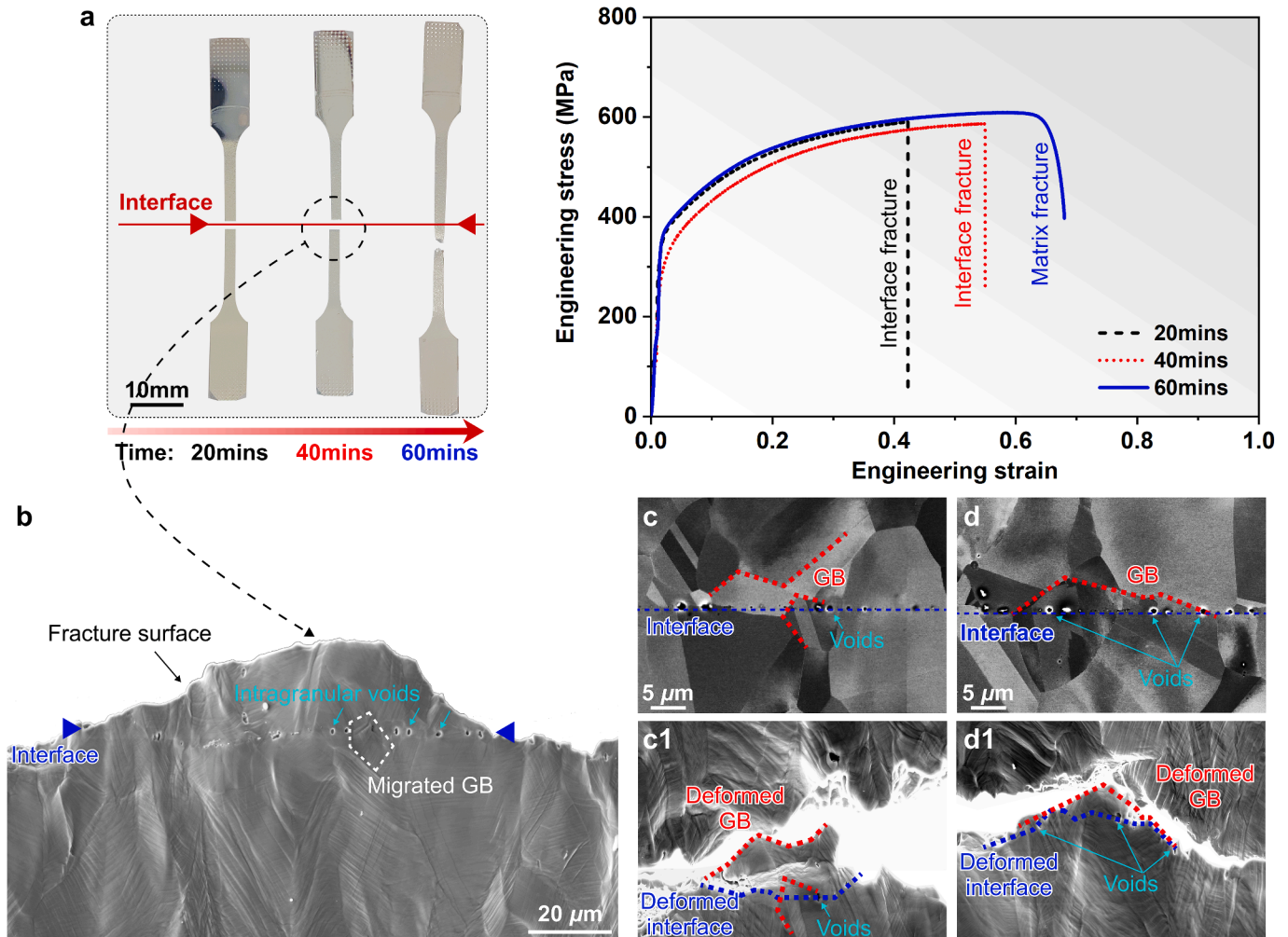


Fig. 5. Tensile fracture behaviours (a) fractured samples fabricated by 900 °C DB and their stress-strain curves, (b) micro-level fracture surface where fracture surface did not pass through the interface voids, (c)/(c1) and (d)/(d1) compares the micro-level fracture surface before and after tensile tests.

the micro-scale do not pass through the DB interface, especially when GB migration occurs with Intragranular voids (see white dot line in Fig. 5b). This is demonstrated in Fig. 5b, that the local fracture surface passes through the matrix rather than the bonding interface, though unclosed interfacial voids still exist at the interface. Around these voids, no obvious severe local plastic deformation can be seen. The same evidence can be obtained by comparing local microstructure before and after tensile tests, as shown in Fig. 5c/c1 and Fig. 5d/d1. These findings demonstrate the complex effects of GB migration on fracture behaviour.

3.3. In-situ observation of the local deformation

To clarify the interaction of GB migration across voids and how they accommodate the local plastic deformation under 900 °C-40mins bonding conditions, specimens with intergranular voids and intragranular voids were designed. These two specimens were in-situ micromechanical tested and characterised by FSE/EBSD, which provides the morphologies of GBs, size of voids, grain orientations, surface dislocation slip lines, and lattice curvature. These two cases were also simulated by CPFE to provide more in-depth analyses of the local stress by accounting for the local void sizes and the anisotropy of grain orientations.

Regarding the case of intergranular voids, a void is located at the interface GBs, surrounded by three grains (Fig. 6a-b), whereas, in case 2, the void is included within a grain due to the GB migration (Fig. 6d). To considering the local grain anisotropy, the Schmid Factors of

surrounding grains are shown with the corresponding slip trace (Fig. 6b and e). The Grain Orientation Spread (GOS) values are adopted to identify the Rx grains with the threshold value of 1.0°, as shown in Fig. 6c and f.

Figs. 7 and 8 exhibit the in-situ observations of interfacial intergranular and intragranular voids, respectively. Fig. 7 presents the interfacial intergranular void's in-situ FSE/EBSD micrographs at four tensile testing stages. As shown in Fig. 7a to d, slight slip traces can be seen in some of the Rx grains when the global stress achieves 350 MPa, indicating that the monitored region of interest undergoes mild plastic deformation. Although the grains surrounding the target void do not show evident slip traces, the observed surface around the void turns slightly uneven, indicating the onset of plasticity. As the stress level increases to ~400 MPa, a large plastic flow occurs around the void, as highlighted by cyan arrows in the FSE image (Fig. 7c). Apparent slip traces are found in the surrounding grains when the interface is stressed to 450 MPa. At this stage, the free surface became uneven, suggesting the typical 'orange peels' phenomenon caused by the out-plane strain component.

Lattice curvature within grains, raised by the strain gradient and measured as kernel average misorientation (KAM), indicates local plasticity and homogeneity. Thus, KAM maps are calculated from the captured in-situ EBSD orientation maps, considering the 3rd nearest neighbouring pixels with a maximum misorientation of 5°. In the initial undeformed DBed sample, as seen in Fig. 7e, low KAM is found in Rx grains, which have undergone recrystallisation during DB. A few non-Rx

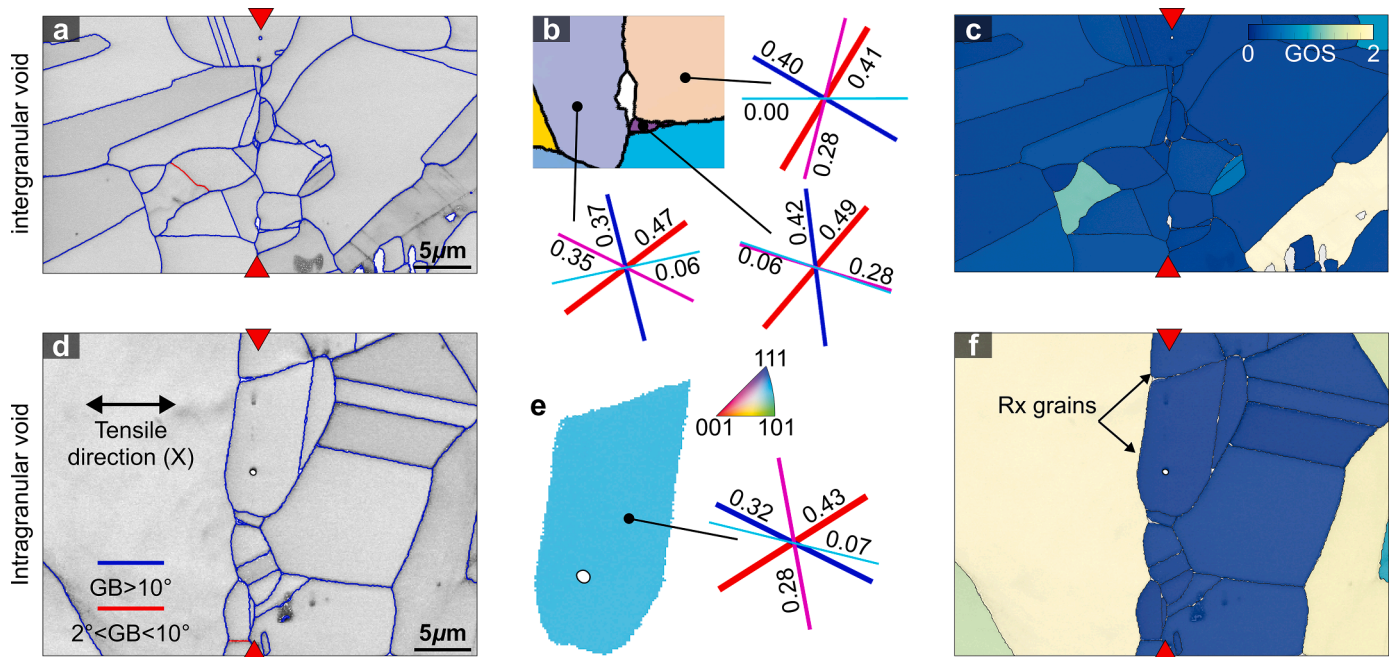


Fig. 6. Microstructure details of in-situ monitored regions (a) and (d) grain boundary map overlaid with band contrast map to show grain morphology; (b) and (e) IPF map of surrounding grains with Schmid Factor of each slip trace; (c) and (f) GOS map to identify Rx and non-Rx grains. (a), (b) and (c) refer to the intergranular void; (d), (e) and (f) refer to the intragranular void.

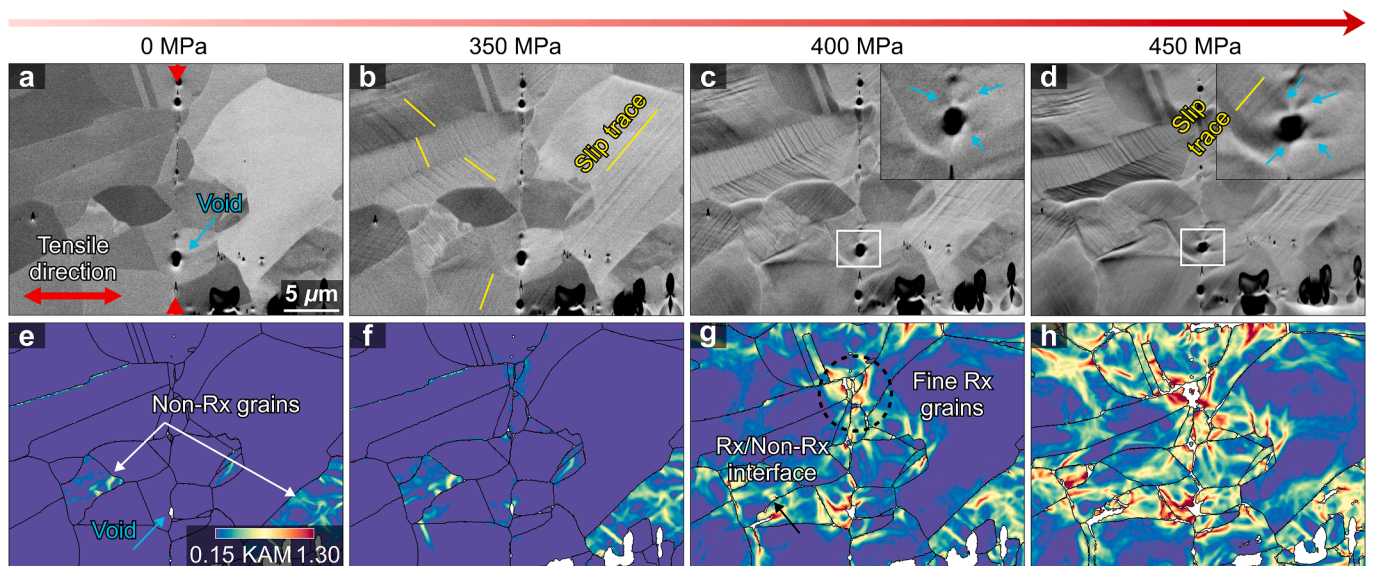


Fig. 7. In-situ observations at the intergranular void where the void is located at the interface GB. (a) to (d) FSE images and (e) to (h) KAM maps from EBSD.

grains can also be found.

As the applied stress increases to 350 MPa, local plastic flow occurs, and higher KAM values appear at the interfacial intergranular void, indicating more significant plastic flow. As the tensile stress level further increases, higher KAM points emerge from the fine grains, triple junctions, and the Rx/non-Rx GBs joints, likely due to the highly inhomogeneous yield strength in various grain sizes and various dislocation contents with the Rx and Non-Rx grains. Compared to these fine grains, triple junction and voids, higher KAM points are still around the intergranular voids, as shown in Fig. 7g. Such trends continue at 450 MPa tensile load.

Regarding the interfacial intragranular voids case, in which the interfacial GBs migrate across and include the voids, the results of the in-situ micromechanical investigation are shown in Fig. 8. At the early

stage of tensile loading, clear slip lines appear firstly in Rx grains, and large plastic flow is found near the GBs. Nevertheless, the KAM value near the void is low. As the tensile load increases, regions near the GBs undergo significantly inhomogeneous plastic flow. Still, no sign of high KAM near the void is found in Fig. 8g (400 MPa) and Fig. 8h (450 MPa).

In summary, for the case without GB migration (intergranular voids), the severer heterogeneous plastic deformation occurred near the void, considerably higher than that around GBs or triple junctions. In contrast, in the case of GB migration across voids (intragranular voids), the deformation heterogeneity around the void is only moderate, at a similar level to that of around the GBs, as demonstrated by the slip line analysis, presented in Fig. 8b c and d.

Note that the grain level plasticity is complex. It is affected by the GB migration and voids and by complex crystallographic and geometrical

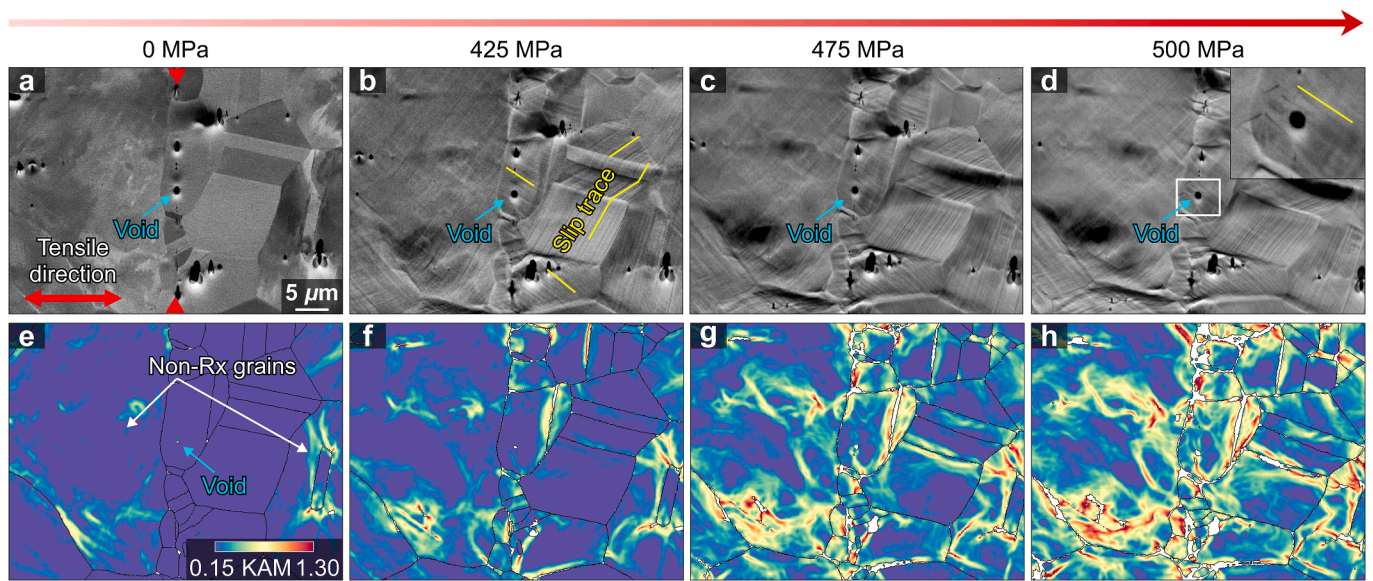


Fig. 8. In-situ observations at the intragranular void where the GB migration appears, and void located within the grain. (a) to (d) FSE images and (e) to (h) KAM maps from EBSD.

features such as crystallographic orientations, grain sizes, grains and void morphologies, the void size, and so on. Thus, the obtained results should be treated with caution as the weights of these factors on plastic deformation are unknown. Experimentally controlling these local microscopic variables to determine their weights is extremely hard. Nevertheless, these microscopic variables can be systematically controlled and analysed using the CPFE approach, establishing the sole relationship between GB migration across voids and local plastic deformation. Thus, systematic bi-crystal CPFE analyses are conducted to investigate this issue further.

3.4. Dislocation-based crystal plasticity modelling

To account for the local plastic anisotropy effects caused by grain orientations, the worst scenario (largest stress raised by grain orientation mismatch) is created by modelling a ‘hard’-‘soft’ grain pair, for which the Schmid factor is used as an indicator of the yield strength of individual grain. In this case, the ‘hard’ grain has a very low Schmid Factor of 0.31, a hard orientation for dislocation to slip. In contrast, the ‘soft’ grain has a very high Schmid factor of 0.50, a soft and easy-to-slip orientation to the loading axis X. All other variables, such as the void sizes and grain morphologies, are kept constant. The loading and boundary conditions of the bi-crystal CPFE models are shown in Fig. 9a, and the details of the modelling method are described in the Method section.

Three cases, namely, the intergranular void between the hard and soft grains, intragranular void within the hard grain, and intragranular voids within the soft grain, are created to clarify the effects of GB migration interaction with voids, as shown in Fig. 9c. The normal stress (σ_{xx}) along the loading axis and geometrically necessary dislocation (GND) density, which is an aggregation of dislocations causing lattice curvature to accommodate the exerted strain gradient, are used as indicators to evaluate the plastic deformation near the voids.

The predicted stress and GND density of the three cases at 1% global strain are shown in Fig. 9b, c and d. The stress contour plots are shown in Fig. 9b1, c1 and d1, and more quantitative analyses of the stress values obtained from the integration points of elements are presented in Fig. 9b2, c2 and d2. As expected, the high stresses are localised at the edge of voids but rapidly drop with Y distance for all three cases. However, the magnitude of the peak stress in the un-migrated (intergranular) case is observed to reach up to ~ 1100 MPa, while the peak

stress of Case B and C (GB migrated to the soft and hard grain) is only ~ 830 MPa (mean value between Case B and C, also see Fig. 11a), suggesting that the stress concentrations are alleviated by GB migration, as shown in Fig. 9c1 and d1.

Similar trends are also observed for the GND distributions; higher GND density is found in the un-migrated case. These high GND density points are found near the edge of the void and GB, as shown in Fig. 9b. The GBs in the polycrystal have been proven to resist the lattice motion dislocations at a moderate plastic strain level [42]. Even though the absorption and GB-dislocation interaction are observed at higher strain levels, the dislocation concentration at the GB is still more marked than within the grain. In the current work, the higher dislocation density is initially induced at the edge of voids due to the geometrically induced plastic strain gradient (Fig. 9c and d). The presence of GB intersecting with the void, as seen in Fig. 9b, exacerbates the dislocation concentration, leading to high normal stresses to the GB plane (Fig. 9b1) and potential crack nucleation. Dakshinamurthy et al. [43] indicated that the presence of intergranular void results in the non-uniform lattice rotation, leading to an increase in lattice curvature. The deformation-induced local misorientation is more pronounced in the case of a ‘hard’-‘soft’ grain pair due to the incompatibility between the two grains. This observation shows good agreement with the present results.

These results suggest that the GB migration seems to be able to alleviate the stress concentration and GND accumulation, thus providing the mechanistic explanation for the observed fracture behaviour shown in Fig. 5. The quantitative analyses of the stress and GND density distribution amongst the three cases is probably the first quantitative investigation of the GB migration effect on local deformation, providing compelling experimental and numerical evidence.

In-depth analyses of the micro-plasticity of GB migration effects are undertaken by examining the slip activities within grains, as illustrated in Fig. 10. The 12 slip systems are represented by twelve red, green, and blue (RGB) colours from the ‘rainbow’ colour key. amongst all 12 slip systems, the shear strain γ^α on slip systems is compared, such that the primary slip system with the maximum γ^α amongst 12 slip systems in each element can be determined and coloured.

In cases of GB migrating across the voids (intragranular voids), either from the soft to the hard grain (Fig. 10a) or from the hard to the soft grain (Fig. 10b), the GB seems to have little influence on the activation of the slip system, probably due to the relatively long distance from the

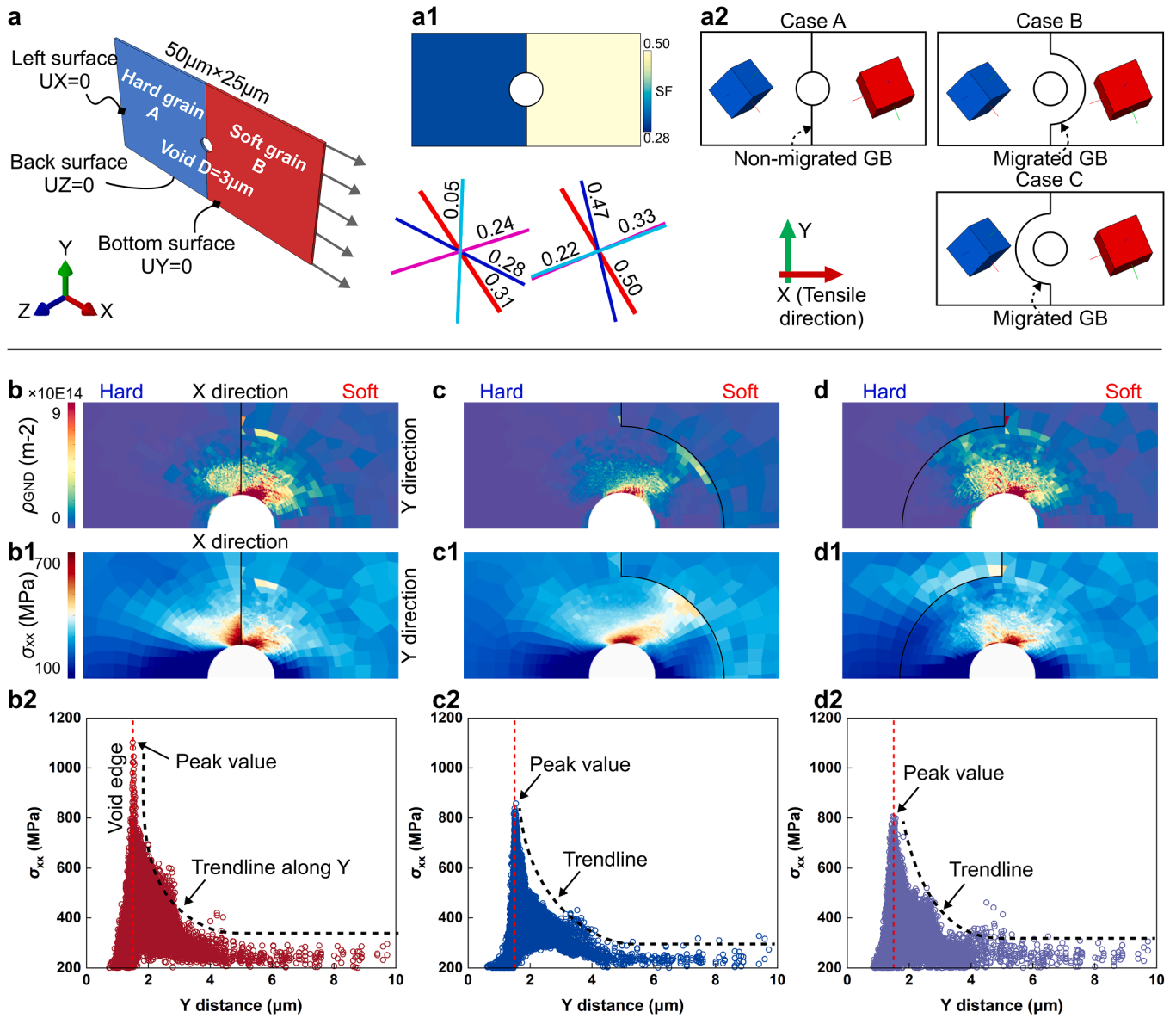


Fig. 9. Bi-crystal CPFEE model and calculation results: (a) boundary conditions, (a1) Schmid factor and slip systems, (a2) three cases with or without GB migration; (b), (c) and (d) are GND and stress distributions with or without GB migration: (b), (b1), (b2) no GB migration occurs; (c), (c1), (c2) GB migrates to the soft grain and (d), (d1), (d2) GB migrates to the hard grain.

top edge of the void, where the stress concentrates, implying that the void size and grain orientations determine the slip activities. For instance, in the case of the migrated interfacial GB within a soft grain, as seen in Fig. 10a, at the upper edge of the void, $(1-11)\langle 10-1 \rangle$ and $(-111)\langle 101 \rangle$ slip systems are activated. The corresponding γ^α distribution is displayed in Fig. 10a1 and a2. The high γ^α region, contributed by multi-slips, is localised near the upper edge of the void, as highlighted by a black dotted line and overlaid with the corresponding slip system in Fig. 10a3.

Such multi-slip activities at the top edge of the voids can also be seen in the case of the void included within the hard grain (Fig. 10b), but the primary and secondary slip systems are different from that of the soft grain. Since the slip interaction has been shown to increase the local GND density significantly in [44], the obtained results in Fig. 10 further explain the high GND density around the edge of voids.

Regarding the case without GB migration (intergranular void), as presented in Fig. 10c, the primary and secondary slip systems are similar to those shown in the cases of GB migration across the voids in Fig. 10a and b, suggesting that the GB migration has little effect on the

dislocation slip activities (plastic flow), which are predominately determined by the grain orientation and void size.

3.5. Comparison of void closure with GB migration

The void closure often is a simultaneous process of GB migration during many manufacturing processes, such as DB in this study, between 40 and 60 min at 900 °C, where both GB migration and void closure occur. The systematic investigation of the effects of void closure on local stress is conducted in this section and compared with the effects of GB migration obtained from the study of the previous section. The overview results are presented in Fig. 11, in which an interfacial void size is reduced from 3 μm to 1.5 μm and 1 μm, corresponding to the 20 mins, 40 mins and 60 mins DB at 900 °C. Noting that void closure is a complex micro deformation and diffusion process [45,46], the closure process would be slower as the size of voids reduces. This matches well with the characterisation results shown in Fig. 4. The grain orientations in all three cases are kept constant by setting them to be the same as a bi-crystal model (Case A). As shown in Fig. 11a, as the void shrinks from

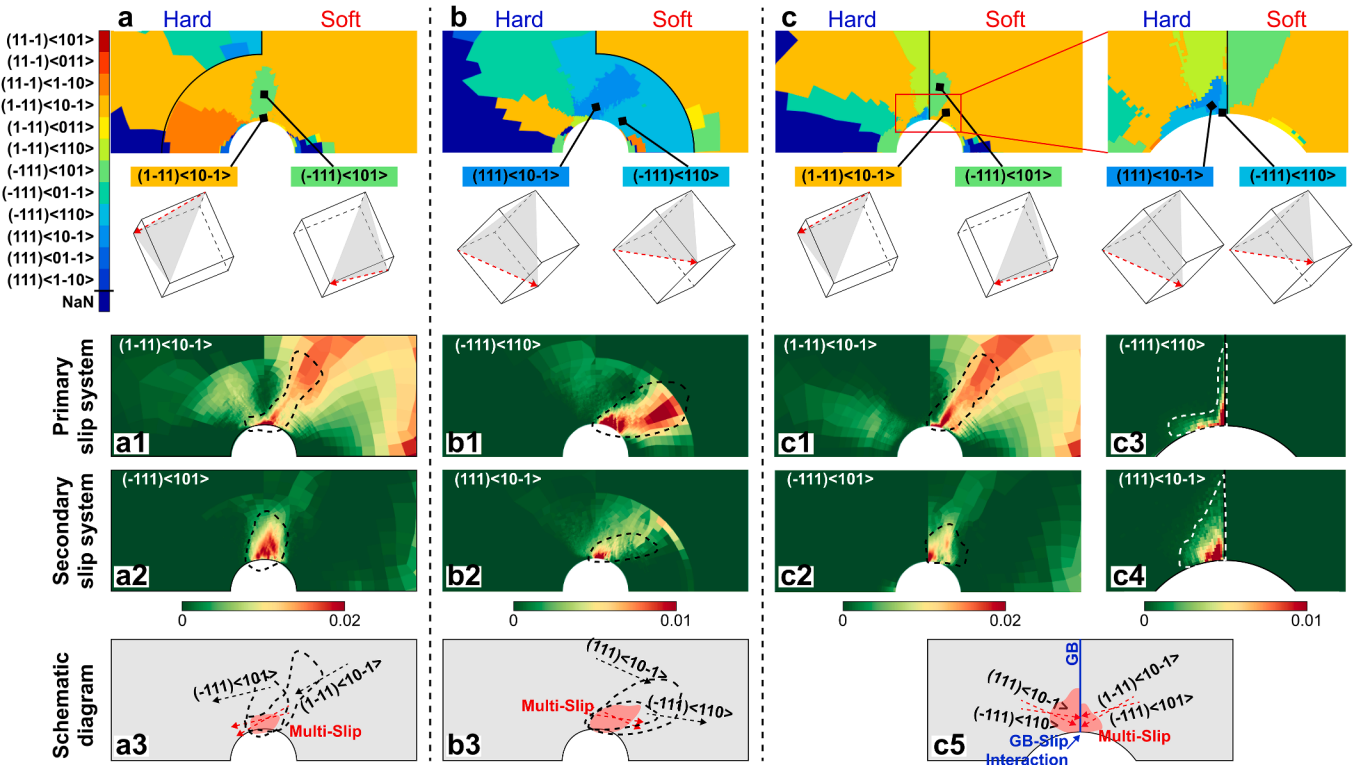


Fig. 10. Slip activation with or without GB migration (a) GB migrates to the hard grain, (b) GB migrates to the soft grain, and (c) no GB migration occurs. (a1), (b1), (c1) and (c3) show primary slip system; (a2), (b2), (c2) and (c4) show secondary slip system; (a3), (b3) and (c5) are schematic diagram of multi-slip interaction.

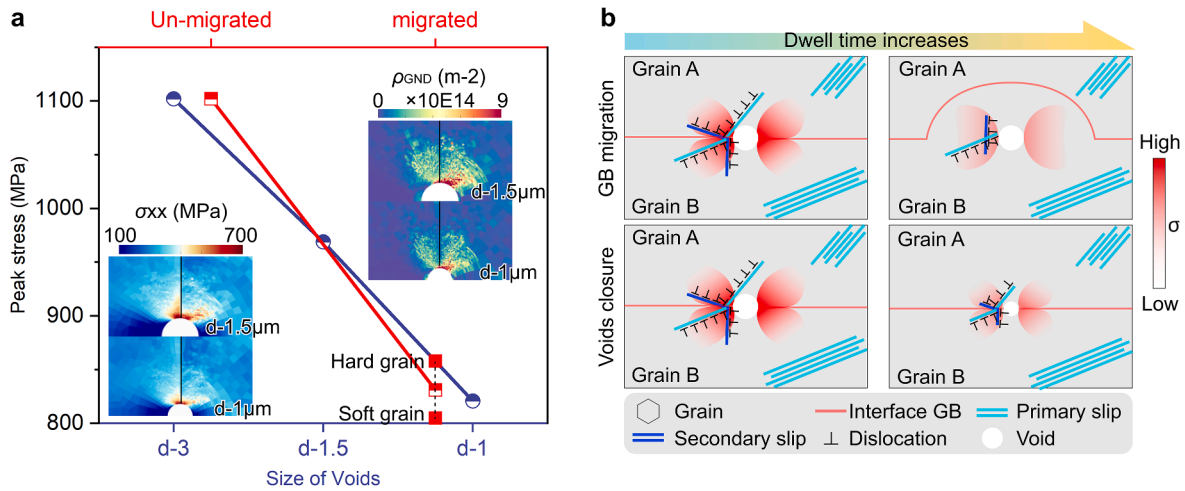


Fig. 11. Comparison between the effects of GB migration and void closure on stress alleviation (a) comparison of the peak stress and (b) schematic of local tensile behaviours affected by the GB migration and voids closure.

3 μm to 1 μm , the peak stress near the edge of the voids drops rapidly from ~ 1100 MPa to ~ 820 MPa. It is of great interest to see that this effect of stress drop is very similar to the GB migration resulting in stress drop (1100 MPa to 830 MPa). Based on the results and discussion presented above, the local deformation mechanism, affected by the GB migration and voids closure, is proposed, summarised, and schematically presented in Fig. 11b.

4. Conclusions

In summary, to investigate the GB migration and void closure effects on local stress variation, 316 L samples DBed under designed

temperature and dwell time, generating various interfacial microstructures. These samples are then in-situ tested to fracture, and the micro-level fracture behaviour suggests the migrated GB's significant effects on local deformation around the interfacial void. It is found that if the interfacial GB migrates across the interfacial voids, although these voids still have relatively large sizes, micro-cracks do not nucleate from them or penetrate through them.

Since the problem is complex due to many microstructural variables, such as grain orientation, GB migration, and voids sizes, systematic quantitative CPFÉ studies are undertaken to provide insights into microstructural features' roles (weight). The models consist of a soft-hard grain paired, a bi-crystal system with a void on the GB in the

central. It is found that GB migration considerably alleviates the stress concentration (from 1100 MPa to 830MPa) around the voids, showing equivalent stress alleviation effects to the voids closure from 3 μ m to 1 μ m. The grain orientation effects, GB migration to the hard or soft grain, is also studied. The grain orientation effect (~50 MPa) on stress alleviation near the voids is significantly less than the GB migration effect (~280 MPa) (Fig. 11a). Also, detailed dislocation slip activities are conducted to provide an in-depth understanding of the plastic flow near voids with various grain orientations. These findings clarify the role of GB migration across voids.

In industrial practice, achieving high reliability for safety-critical parts is essential. Unfortunately, advanced manufacturing processes, such as AM, powder metallurgy (PM) and DB, commonly contain undesired micro-voids. To improve the reliability of as-fabricated parts, extensive research has been conducted on post-processing technologies, such as hot isostatic pressing (HIP) for AM parts. Our work shows that the GB migration across the voids can achieve promising local stress mitigation. The thermal-mechanical conditions used in this work to achieve GB migration are well suited to HIP and PM. The results shown here may open a new avenue for achieving superior mechanical properties of metallic parts, guiding the new process design.

CRedit authorship contribution statement

W.W. and J.J. contributed to the overall idea behind the investigation. W.W. implemented the in-situ tensile tests and CPFPE simulations. A.A.S. carried out the diffusion bonding tests. W.W., J.J., D.S.B. L.A., A.A.S., Y.W. and J.L. contributed to the critical discussion of the results and the writing of the manuscript.

Declaration of Competing Interest

The authors declare that they have no known competing financial interests or personal relationships that could have appeared to influence the work reported in this paper.

Acknowledgements

This work has been part-funded by the EPSRC Energy Programme (grant number EP/W006839/1). WW gratefully acknowledges the China Scholarship Council (grant number 202006050025) for financial support through the Imperial-CSC scholarship scheme. The authors thank Dr Yang Liu from Imperial College London for useful discussions on CPFPE modelling.

References

- [1] M. Qu, et al., Controlling process instability for defect lean metal additive manufacturing, *Nat. Commun.* 13 (2022) 1079.
- [2] S. Noh, R. Kasada, A. Kimura, Solid-state diffusion bonding of high-Cr ODS ferritic steel, *Acta Mater.* 59 (2011) 3196–3204.
- [3] Z.L. Ma, S.A. Belyakov, K. Sweatman, T. Nishimura, T. Nishimura, C.M. Gourlay, Harnessing heterogeneous nucleation to control tin orientations in electronic interconnections, *Nat. Commun.* 8 (2017) 1916.
- [4] S. Kurian, R. Mirzaeifar, Selective laser melting of aluminum nano-powder particles, a molecular dynamics study, *Addit. Manufact.* 35 (2020), 101272.
- [5] W.W. Basuki, O. Kraft, J. Aktaa, Optimization of solid-state diffusion bonding of Hastelloy C-22 for micro heat exchanger applications by coupling of experiments and simulations, *Mater. Sci. Eng.: A* 538 (2012) 340–348.
- [6] C. Zhang, H. Li, M.Q. Li, Interaction mechanism between void and interface grain boundary in diffusion bonding, *Sci. Technol. Weld. Join.* 20 (2015) 123–129.
- [7] D.D. Gu, W. Meiners, K. Wissenbach, R. Poprawe, Laser additive manufacturing of metallic components: materials, processes and mechanisms, *Int. Mater. Rev.* 57 (2012) 133–164.
- [8] W.E. Frazier, Metal additive manufacturing: a review, *J. Mater. Eng. Perform.* 23 (2014) 1917–1928.
- [9] T. Yalçınkaya, İ.T. Tandoğan, İ. Özdemir, Void growth based inter-granular ductile fracture in strain gradient polycrystalline plasticity, *Int. J. Plast.* 147 (2021), 103123.
- [10] T. Vigraman, R. Narayanasamy, D. Ravindran, Microstructure and mechanical property evaluation of diffusion-bonded joints made between SAE 2205 steel and AISI 1035 steel, *Mater. Des.* 35 (2012) 156–169.

- [11] Y. Wang, X.Q. Cai, Z.W. Yang, D.P. Wang, X.G. Liu, Y.C. Liu, Diffusion bonding of Ti2AlNb alloy using pure Ti foil as an interlayer, *J. Alloys Compd.* 756 (2018) 163–174.
- [12] S. Afshan, D. Balint, D. Farrugia, J. Lin, A new experimental method for identifying the conditions necessary for diffusion bonding in free cutting steels, *Mater. Sci. Eng.: A* 586 (2013) 25–30.
- [13] J. Zhang, D. Xie, Q. Li, C. Jiang, Q. Li, Effect of holding time on the microstructure and strength of tungsten/steel joints by HIP diffusion bonded using a Cu interlayer, *Mater. Lett.* 261 (2020), 126875.
- [14] Z. Du, S. Jiang, K. Zhang, Z. Lu, B. Li, D. Zhang, The structural design and superplastic forming/diffusion bonding of Ti2AlNb based alloy for four-layer structure, *Mater. Des.* 104 (2016) 242–250.
- [15] C-w Wang, T. Zhao, G. Wang, J. Gao, H. Fang, Superplastic forming and diffusion bonding of Ti–22Al–24Nb alloy, *J. Mater. Process. Technol.* 222 (2015) 122–127.
- [16] C. Zhang, H. Li, M. Li, Role of surface finish on interface grain boundary migration in vacuum diffusion bonding, *Vacuum* 137 (2017) 49–55.
- [17] X. Shao, X. Guo, Y. Han, W. Lu, J. Qin, D. Zhang, Characterization of the diffusion bonding behavior of pure Ti and Ni with different surface roughness during hot pressing, *Mater. Des.* (1980-2015) 65 (2015) 1001–1010.
- [18] B. Wei, W. Wu, D. Xie, M. Nastasi, J. Wang, Strength, plasticity, thermal stability and strain rate sensitivity of nanograined nickel with amorphous ceramic grain boundaries, *Acta Mater.* 212 (2021), 116918.
- [19] R.J. Bourcier, D.A. Koss, R.E. Smelser, O. Richmond, The influence of porosity on the deformation and fracture of alloys, *Acta Metall.* 34 (1986) 2443–2453.
- [20] L. Wang, et al., Grain rotation mediated by grain boundary dislocations in nanocrystalline platinum, *Nat. Commun.* 5 (2014) 4402.
- [21] S. Kondo, A. Ishihara, E. Tochigi, N. Shibata, Y. Ikuhara, Direct observation of atomic-scale fracture path within ceramic grain boundary core, *Nat. Commun.* 10 (2019) 2112.
- [22] S. Chu, et al., In situ atomic-scale observation of dislocation climb and grain boundary evolution in nanostructured metal, *Nat. Commun.* 13 (2022) 4151.
- [23] V. Prithivirajan, M.D. Sangid, The role of defects and critical pore size analysis in the fatigue response of additively manufactured IN718 via crystal plasticity, *Mater. Des.* 150 (2018) 139–153.
- [24] M. Diehl, M. Wicke, P. Shanthraj, F. Roters, A. Brueckner-Foit, D. Raabe, Coupled crystal plasticity–phase field fracture simulation study on damage evolution around a void: pore shape versus crystallographic orientation, *JOM* 69 (2017) 872–878.
- [25] W. Zhang, et al., Very-high-cycle fatigue behavior of AlSi10Mg manufactured by selected laser melting: crystal plasticity modeling, *Int. J. Fatigue* 145 (2021), 106109.
- [26] H.-J. Guo, C. Ling, E.P. Busso, Z. Zhong, D-F. Li, Crystal plasticity based investigation of micro-void evolution under multi-axial loading conditions, *Int. J. Plast.* 129 (2020), 102673.
- [27] B. Xie, et al., Oxidation of stainless steel in vacuum and evolution of surface oxide scales during hot-compression bonding, *Corros. Sci.* 147 (2019) 41–52.
- [28] F.P.E. Dunne, D. Rugg, A. Walker, Lengthscale-dependent, elastically anisotropic, physically-based hcp crystal plasticity: application to cold-dwell fatigue in Ti alloys, *Int. J. Plast.* 23 (2007) 1061–1083.
- [29] F.P.E. Dunne, R. Kiwanuka, A.J. Wilkinson, Crystal plasticity analysis of micro-deformation, lattice rotation and geometrically necessary dislocation density, *Proceed. Roy. Soc. A: Math. Phys. Eng. Sci.* 468 (2012) 2509–2531.
- [30] C.A. Sweeney, B. O'Brien, F.P.E. Dunne, P.E. McHugh, S.B. Leen, Strain-gradient modelling of grain size effects on fatigue of CoCr alloy, *Acta Mater.* 78 (2014) 341–353.
- [31] Caillard D., Martin J.-L. *Thermally Activated Mechanisms in Crystal Plasticity.* Elsevier (2003).
- [32] G.I. Taylor, The mechanism of plastic deformation of crystals. Part II.—comparison with observations, in: *Proceedings of the Royal Society of London Series A, Containing Papers of a Mathematical and Physical Character* 145, 1934, pp. 388–404.
- [33] C. Paramatmuni, Y. Guo, P.J. Withers, F.P.E. Dunne, A three-dimensional mechanistic study of the drivers of classical twin nucleation and variant selection in Mg alloys: a mesoscale modelling and experimental study, *Int. J. Plast.* 143 (2021), 103027.
- [34] A. Arsenlis, D.M. Parks, Crystallographic aspects of geometrically-necessary and statistically-stored dislocation density, *Acta Mater.* 47 (1999) 1597–1611.
- [35] J.F. Nye, Some geometrical relations in dislocated crystals, *Acta Metall.* 1 (1953) 153–162.
- [36] J. Cheng, S. Ghosh, A crystal plasticity FE model for deformation with twin nucleation in magnesium alloys, *Int. J. Plast.* 67 (2015) 148–170.
- [37] Z. Zhang, D. Lunt, H. Abdolvand, A.J. Wilkinson, M. Preuss, F.P.E. Dunne, Quantitative investigation of micro slip and localization in polycrystalline materials under uniaxial tension, *Int. J. Plast.* 108 (2018) 88–106.
- [38] Y. Liu, F.P.E. Dunne, The mechanistic link between macrozones and dwell fatigue in titanium alloys, *Int. J. Fatigue* 142 (2021), 105971.
- [39] C. Paramatmuni, F.P.E. Dunne, Effect of twin crystallographic orientation on deformation and growth in Mg alloy AZ31, *Int. J. Plast.* 135 (2020), 102775.
- [40] C. Hardie, R. Thomas, Y. Liu, P. Frankel, F. Dunne, Simulation of crystal plasticity in irradiated metals: a case study on Zircaloy-4, *Acta Mater.* 241 (2022), 118361.
- [41] B. Chen, K.G.F. Janssens, F.P.E. Dunne, Role of geometrically necessary dislocation density in multiaxial and non-proportional fatigue crack nucleation, *Int. J. Fatigue* 135 (2020), 105517.
- [42] S. Sun, B. Adams, W. King, Observations of lattice curvature near the interface of a deformed aluminium bicrystal, *Philos. Mag.* A 80 (2000) 9–25.

- [43] M. Dakshinamurthy, K. Kowalczyk-Gajewska, G. Vadillo, Influence of crystallographic orientation on the void growth at the grain boundaries in bicrystals, *Int. J. Solids Struct.* 212 (2021) 61–79.
- [44] B. Poole, F.P.E. Dunne, Slip band interactions and GND latent hardening in a galling resistant stainless steel, *Mater. Sci. Eng.: A* 813 (2021), 141176.
- [45] A. Hill, E.R. Wallach, Modelling solid-state diffusion bonding, *Acta Metall.* 37 (1989) 2425–2437.
- [46] B. Derby, E.R. Wallach, Theoretical model for diffusion bonding, *Metal Sci.* 16 (1982) 49–56.